



23 discrepancies, particularly during the spring and summer seasons; convective
24 precipitation exhibits greater regional and seasonal variability than stratiform
25 precipitation. Furthermore, the findings indicate that aerosols exert an influence on
26 precipitation through microphysical processes, encompassing the growth via
27 condensation on cloud condensation nuclei, coalescence growth, semi-direct effect,
28 and moisture competition. These phenomena exhibit distinct variations that are
29 influenced by spatial and temporal factors, as well as the particular type of aerosols
30 present. Specifically, convective precipitation in the BTH region is dominated by the
31 semi-direct effect of dust aerosols, whereas the YRD and PRD are more influenced
32 by hygroscopic sea salt aerosols and the YRM by fine aerosol particles. Furthermore,
33 RH promotes condensation and coalescence processes by replenishing water vapor,
34 particularly under low aerosol loading. However, CAPE plays a dual role: it enhances
35 precipitation by intensifying cloud development and suppresses it through particle
36 break-up driven by dynamics. The present study elucidates the mechanisms of
37 spatio-temporal modulation underlying aerosol-precipitation interactions, offering a
38 scientific foundation for the refinement of climate models within urban
39 agglomerations.

40 **Key words:** GPM DPR, MERRA-2, Aerosols, Precipitation Structure, Urban
41 Agglomerations

42

43



44 1. Introduction

45 Aerosols modulate clouds and precipitation primarily through Aerosol–Radiation
46 Interactions (ARI) and Aerosol–Cloud Interactions (ACI). These mechanisms affect
47 the intensity, frequency, and spatiotemporal distribution of precipitation (Rosenfeld et
48 al., 2008). These processes involve complex multiscale, multi–factor coupling effects
49 with profound implications for regional hydrological cycles, extreme weather events,
50 and climate systems (Li et al., 2016, 2019; Ramanathan et al., 2001). Therefore, one
51 of the most important problems facing atmospheric research is the clarification of
52 aerosol–driven precipitation mechanisms (IPCC, 2013; IPCC, 2021). In this
53 framework, the ACI describes the mechanism by which aerosols function as ice nuclei
54 (IN) and cloud condensation nuclei (CCN), modifying cloud microphysical processes
55 to indirectly modify the type and distribution of precipitation intensity (Gettelman,
56 2015). These include cloud droplet spectrum distribution, phase transition efficiency,
57 and precipitation formation pathways (Xie et al., 2013). Known as the Twomey Effect
58 (the First Indirect Effect), higher aerosol concentrations increase the number of cloud
59 droplets, while decreasing their effective radius (r_e) and increasing cloud albedo
60 (Twomey, 1974). In addition, the Cloud Lifetime Effect (Second Indirect Effect),
61 aerosol-induced reduction in r_e suppresses precipitation initiation, whereas
62 prolonging cloud lifetime (Albrecht, 1989). The Semi-Direct Effect is another way in
63 which absorptive aerosols can shorten cloud lifetime by heating the atmosphere
64 through the absorption of shortwave radiation, which accelerates droplet evaporation
65 (Ackerman et al., 2000; Huang et al., 2014). There are still many unknowns



66 surrounding the measurement of aerosol impacts on precipitation, even though the
67 primary mechanisms of aerosol–precipitation interactions are documented. This is due
68 to the diversity and highly nonlinear characteristics of aerosol–precipitation responses
69 (Chang et al., 2015), which are jointly regulated by aerosol concentration, type,
70 vertical distribution, and local meteorological conditions (Fan et al., 2007; Storer et al.,
71 2010), leading to pronounced regional variations (Xiao et al., 2025). Furthermore,
72 external synoptic conditions modulate the ACI process (Chen et al., 2025; Sun et al.,
73 2023; Zhao et al., 2024).

74 Significant research in recent years has focused on aerosol–induced modifications
75 of precipitation structures in key regions of China. Major urban agglomerations,
76 Beijing–Tianjin–Hebei (BTH), Yangtze River Delta (YRD), Pearl River Delta (PRD),
77 and Yangtze River Middle Reaches (YRM)–represent China’s most economically
78 vibrant and densely populated areas while also experiencing severe aerosol pollution
79 (Guo et al., 2018; Sun and Zhao, 2021; Zhao et al., 2025), thus providing critical entry
80 points for investigating regional manifestations of aerosol effects. Although previous
81 research has been conducted on precipitation patterns in more general areas such as
82 the North China Plain (Sun et al., 2023), South China (Chen et al., 2025), and East
83 China (Wen et al., 2023), analysis of specific seasons or precipitation types is
84 frequently limited without considering meteorological drivers. Moreover, numerical
85 models show substantial instability in precipitation capture (Zhang et al., 2024), and
86 simulation capabilities exhibit inherent asymmetries (Snively and Gallus, 2014). In
87 summary, methodological divergences and data source variations across studies have



88 yielded divergent conclusions with persistent controversies, precluding robust
89 cross-regional comparisons of aerosol impacts on precipitation structures. Therefore,
90 it is essential to develop consistent techniques for the collection and interpretation of
91 aerosol-precipitation data.

92 The Global Precipitation Measurement (GPM) mission extends and advances the
93 Tropical Rainfall Measuring Mission (TRMM). Compared with TRMM's
94 single-frequency Precipitation Radar (PR), the Dual-frequency Precipitation Radar
95 (DPR) onboard the GPM core observatory demonstrates higher sensitivity and
96 provides more accurate three-dimensional precipitation structure. This increase
97 markedly enhances precipitation detection capabilities at mid-to high latitudes (Hou et
98 al., 2014). Furthermore, comparisons between GPM DPR precipitation data and
99 observations from ground-based radars and meteorological stations (Chandrasekar
100 and Le, 2015; Lasser et al., 2019; Sun et al., 2020) validated the substantial agreement
101 across all three platforms. Moreover, a robust concordance in surface precipitation
102 patterns and brilliant band height was noted between DPR data and the
103 high-resolution NICAM 3.5 km model (Kotsuki et al., 2023), hence reinforcing data
104 dependability.

105 Additionally, Modern-Era Retrospective Analysis for Research and Applications
106 Version 2 (MERRA-2) significantly improves the accuracy of aerosol vertical
107 distributions and optical properties through assimilation of multi-source satellite and
108 ground-based observations (Buchard et al., 2017; Chang et al., 2015). Building on the
109 reliable precipitation data from GPM DPR, researchers analyzed aerosol impacts on



110 precipitation vertical structure, microphysical characteristics, and extreme
111 hydrometeorological events using integrated MERRA-2 aerosol and DPR
112 precipitation datasets (Ji and Tian, 2024; Jiang et al., 2023; Sun et al., 2022).
113 Furthermore, compared with the ECMWF Re-Analysis-Interim (ERA-Interim), the
114 European Centre for Medium-Range Weather Forecasts Reanalysis Version 5
115 (ERA-5) offers significantly improved spatiotemporal resolution, yielding superior
116 environmental parameters (Zhao et al., 2021). This enhancement facilitates its
117 widespread utilization in research investigating the impact of aerosol on precipitation
118 structure (Dong et al., 2018; Guo et al., 2018; Pravia-Sarabia et al., 2023).

119 Peng et al. (2025) conducted a focused investigation into the effects of fine and
120 coarse aerosols on summer precipitation processes within the YRD region. The results
121 indicated that coarse aerosols suppress convective precipitation by competing for
122 moisture, whereas fine aerosols enhance precipitation by forming small droplet
123 clusters with condensational and coalescence growth. However, precipitation
124 characteristics vary significantly across different regions and seasons, which can be
125 attributed to differences in aerosol types, concentrations, and meteorological
126 conditions. Therefore, this study integrates precipitation, aerosol, and environmental
127 data from four major urban agglomerations (the BTH, YRD, YRM, and PRD)
128 between 2014 and 2023. A multi-source DPR-MERRA-2-ERA5 dataset was
129 constructed to systematically analyze the impact of aerosol on precipitation properties
130 and microphysical processes. In addition, the interactions between aerosol and
131 precipitation structures are further investigated under varying thermodynamic and



dynamic conditions. This unified methodology facilitates a comprehensive examination of aerosol effects on the precipitation structure and cloud microphysics across China's major urban agglomerations, enabling cross-regional comparative assessments.

The remainder of this paper is organized as follows. Section 2 introduces the data and methods. Section 3 examines aerosol influences on precipitation structure and properties. Section 4 conducts an analysis of aerosol effects on the microphysical processes of precipitation. Section 5 investigates meteorological effects on aerosol-precipitation interactions. Section 6 summarizes the conclusions of this study and Section 7 discusses the limitations and shortcomings of this research.

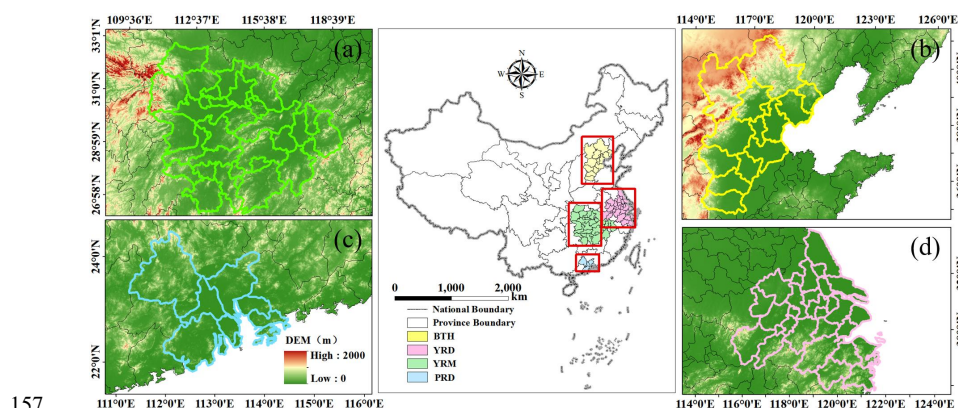
2. Data and Methods

2.1 Study area

The YRM urban cluster (Fig. 1a) is situated between 26°N–32.5°N and 110.5°E–118.3°E, inside a humid subtropical monsoon region characterized by concentrated summer precipitation. The BTH region (36°N–41.6°N, 113.5°E–119.9°E; Fig. 1b) exhibits a temperate semi-humid continental monsoon climate, with summer comprising over 67% of the annual precipitation and spring characterized by numerous dust events (Zhai et al., 2022). The PRD cluster (21.7°N–23.8°N, 112°E–115.4°E; Fig. 1c) exhibits a South Asian tropical marine monsoon climate, characterized by the 85% of annual precipitation occurring from April to September, frequently exacerbated by typhoons (Guo et al., 2018). Dominated by the Taihu Plain



153 (27.9°N–33.3°N, 117.5°E–122.7°E; Fig. 1d), the YRD exhibits a humid subtropical
 154 monsoon climate characterized by concentrated spring–summer precipitation,
 155 including prolonged June–July Meiyu–front rainfall (Liu et al., 2017). Fig. 1 shows
 156 the spatial distribution of all four urban agglomerations.



157 **Fig. 1.** Geographical location and elevation map of the Yangtze River Middle
 158 Reaches (a), Beijing–Tianjin–Hebei (b), Pearl River Delta (c), and Yangtze River
 159 Delta (d) urban agglomeration (source: GS(2024) 0650). Publisher’ s remark: please
 160 note that the above figure contains disputed territories.
 161

162 **2.2 GPM DPR Precipitation Data**

163 Mounted on the core satellite, the DPR transmits at the Kuband (13.6 GHz) and
 164 Kaband (35.5 GHz) frequencies, achieving a nadir horizontal resolution of 5 km to
 165 detect three–dimensional precipitation structures from the surface to an altitude of 22
 166 km (Hou et al., 2014). This study utilized the GPM Level 2 DPR (2ADPR) standard
 167 product, Version 07, which employs two unique antenna scanning modes: the
 168 High–Sensitivity Scan (HS) and the Full Scan (FS). A significant alteration in Version
 169 07, compared to Version 06, entails a shift in the KaPR scanning pattern from the



170 inner swath to the outer swath configuration. This change aligns the KaPR scanning
171 mode with that of KuPR.

172 Given the relatively low frequency of winter precipitation events and frequent
173 occurrence of solid precipitation in northern regions, this study focuses on
174 precipitation data during spring (March–May), summer (June–August), and autumn
175 (September–November) from 2014 to 2023. The parameters analyzed in this study
176 include: The near–surface Rain Rate (nsRR), Rain Rate (RR), Storm Top Height
177 (STH), Liquid Water Path (LWP), Ice Water Path (IWP), DSD, and radar reflectivity
178 factor (Z_e). The DSD includes two parameters: mass–weighted diameter (D_m) and
179 normalized DSD intercepts (N_w).

180 **2.3 MERRA–2 Aerosol Data**

181 This study utilized the MERRA–2 atmospheric reanalysis dataset, updated in
182 2017 and released by NASA's Global Modeling and Assimilation Office (GMAO).
183 By assimilating multi–source observations with numerical modeling techniques, this
184 dataset characterizes the column mass concentrations of five aerosol types: dust (DU),
185 sea salt (SS), sulfate (SO₄), black carbon (BC), and organic carbon (OC), and their
186 corresponding AOD. The data feature a global spatial coverage at a horizontal grid
187 resolution of 0.625°×0.5° (longitude×latitude), with temporal products available at
188 hourly intervals.

189 It is noteworthy that the aerosol data matched are those prior to precipitation
190 events.



191 **2.4 ERA-5 Data**

192 Environmental data for this study were acquired from the ERA5 reanalysis
193 dataset. Through the coupled assimilation of multi-source satellite observations,
194 ground-based measurements, and numerical forecasting systems, this product
195 provides multidimensional climate parameters that span the surface-to-stratopause
196 column (Hersbach et al., 2020). This investigation utilizes two key parameters:
197 Relative Humidity (RH) at 850hPa and Convective Available Potential Energy
198 (CAPE).

199 **2.5 Classification Methods**

200 Prior to data analysis, the DPR, MERRA-2, and ERA5 datasets were subjected to
201 spatiotemporal matching using the best-proximity method. Subsequently,
202 precipitation pixels were screened using the connectivity method (Hu et al., 2022),
203 applying a minimum threshold of four contiguous pixels to define valid precipitation
204 systems. This study categorized precipitation into stratiform and convective types
205 based on the 2ADPR classification criteria, excluding shallow convection events from
206 convective precipitation (Liu and Zipser, 2015). Aerosol classification followed the
207 total AOD thresholds: Low AOD, [0, 0.3); Medium AOD, [0.3, 0.6); and High AOD,
208 [0.6, ~). In terms of aerosol classification, BCA, OCA, and SO_{4A} were categorized as
209 fine aerosol particles, whereas SSA and DUA were classified as coarse aerosol
210 particles.

211 Fig. S1 illustrates the cumulative distribution functions (CDFs) of the RH and
212 CAPE throughout the four urban agglomerations for meteorological conditioning.



213 Given the higher similarity in RH distributions among the YRD, YRM, and PRD
 214 versus distinct BTH characteristics, the YRD–YRM–PRD RH data were unified (red
 215 dashed line; Fig. S1a–c). Conversely, the BTH–YRD–YRM exhibited comparable
 216 CAPE distributions, and the PRD showed significantly higher values. Thus, the
 217 BTH–YRD–YRM CAPE data were combined (red dashed line; Fig. S1d–f). To
 218 balance methodological consistency with regional specificity, the classification
 219 strategy implemented distinct groupings: RH was classified separately for the BTH
 220 region, whereas the YRD, YRM, and PRD shared a unified RH classification.
 221 Similarly, CAPE maintained independent classification for the PRD, whereas BTH,
 222 YRD, and YRM employed combined CAPE classification, as visualized by the red
 223 dashed lines in Fig. S1. Moreover, to prevent feature ambiguity from adjacent
 224 samples, three percentile tiers were defined using the CDFs thresholds: low
 225 (0%–30%), medium (35%–65%), and high (70%–100%), with 30–35% and 65–70%
 226 as buffer zones to avoid adjacent–sample ambiguity.

227 **2.6 Normalized difference calculation**

228 In order to quantify regional and seasonal differences in precipitation parameters,
 229 the BTH region and spring season were set as the benchmark for normalizing
 230 variations. The fractional changes ($\text{DIFF}_{\text{region}}$, in %) for each parameter in the YRD,
 231 YRM, and PRD regions relative to BTH were calculated as follows:

$$232 \quad \text{DIFF}_{\text{region}} = \frac{X_{\text{region}} - X_{\text{BTH}}}{X_{\text{BTH}}} * 100\% \quad (1)$$

233 Beyond regional differences, the fractional seasonal changes ($\text{DIFF}_{\text{season}}$, in %)
 234 for precipitation parameters were calculated as:



$$\text{DIFF}_{\text{season}} = \frac{X_{\text{season}} - X_{\text{spring}}}{X_{\text{spring}}} * 100\% \quad (2)$$

where $\text{DIFF}_{\text{region}}$ represents the normalized differences for the YRD, YRM, and PRD relative to BTH, respectively; $\text{DIFF}_{\text{season}}$ denotes the normalized seasonal differences when comparing summer and autumn to spring. X_{BTH} and X_{spring} represent the reference value of the target precipitation parameter in the BTH and spring, respectively. X_{region} denotes the precipitation parameter values for the YRD, YRM, and PRD regions, respectively, and X_{season} represents the precipitation parameter values in the seasons being compared to spring.

3 Influence of aerosols on precipitation structure and properties

3.1 Correlation changes of precipitation parameters with aerosols

To investigate aerosol impacts on convective and stratiform precipitation characteristics across the four urban agglomerations, five precipitation parameters were selected: nsRR, STH, LWP, IWP, and the precipitation efficiency index (PEI). A correlation heat map of the convective precipitation between AOD and these parameters is shown in Fig. 2. The PEI is a crucial metric for measuring the efficiency of precipitation formation in clouds, indicating the effectiveness of converting cloud water into precipitation. Higher PEI values indicate enhanced precipitation efficiency, which is characterized by a greater conversion of cloud water into rainfall. Following Hu et al. (2022) and scaled by 1000 for enhanced readability, PEI is defined as:

$$\text{PEI} = \frac{\text{nsRR}}{\text{CWP}} = \frac{\text{nsRR}}{(\text{LWP} + \text{IWP})} * 1000 \quad (3)$$



255 In the resulting heat map of convective precipitation (Fig. 2), individual cells
256 exhibit Spearman correlation coefficients that quantify the relationship between AOD
257 and key meteorological parameters. For spring convective precipitation (Fig. 2a–c),
258 the BTH exhibits significant negative correlations with the STH and IWP under low
259 aerosol loading, whereas showing a significant positive correlation with PEI. The
260 YRD displays patterns similar to those of the BTH: negative correlations at low
261 aerosol loading shift to positive correlations with precipitation parameters as aerosol
262 loading increases. In contrast, both the YRM and PRD show consistently positive
263 correlations under low aerosol loading (Fig. 2a). However, the PRD demonstrates
264 pronounced negative correlations at moderate loading, whereas the YRM maintains
265 positive correlations at high aerosol loading. Summer (Fig. 2d–g): Under low (high)
266 AOD conditions, consistent positive (negative) correlations prevail across all study
267 regions (Fig. 2d). At moderate aerosol loading levels, the PRD shifts to a negative
268 correlation, whereas the other three regions retain a positive correlation (Fig. 2e).
269 Autumn (Fig. 2g–i): the YRD exhibits pronounced negative correlations under
270 low–to–moderate AOD thresholds. Conversely, the BTH and YRD (PRD)
271 demonstrate positive (negative) correlations under high AOD levels. Overall, the
272 precipitation under varying aerosol loading exhibits pronounced seasonal and regional
273 disparities, demonstrating nonlinear characteristics in their relationships.

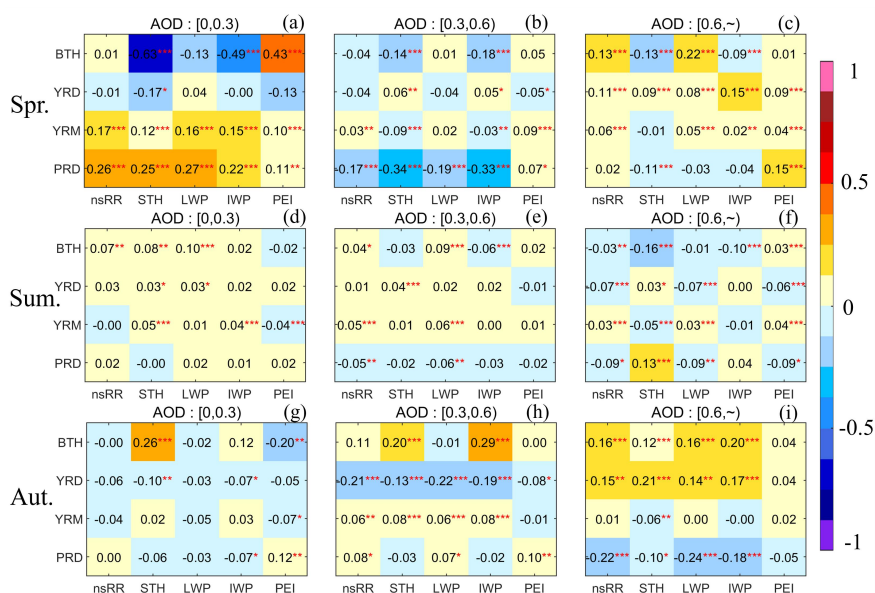


Fig. 2. Spearman correlation coefficients between AOD and precipitation parameters for convective precipitation across regions and seasons under the three AOD regimes. Color gradients (from yellow to blue) encode the correlation strength and direction, and asterisks denote statistical significance (*: $p < 0.05$, **: $p < 0.01$, ***: $p < 0.001$).

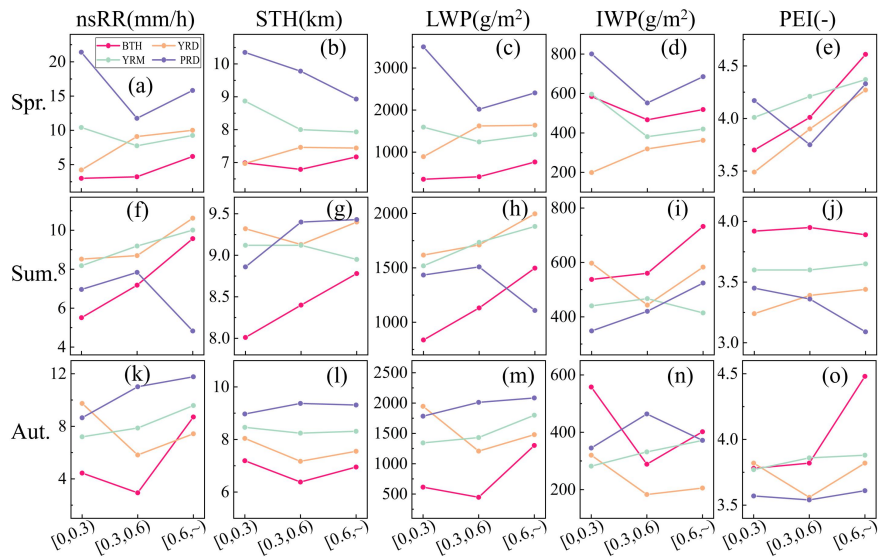
Spearman correlation coefficients are computed to characterize the precipitation parameters in stratiform precipitation (Fig. S3), similar to that of convective precipitation (Fig. 2). Overall, the PRD exhibits the strongest similarity between the stratiform and convective precipitation parameters in the correlation with AOD. In contrast, the BTH, YRD, and YRM resemble convective precipitation characteristics under moderate to high aerosol loading, but show reduced similarity under low aerosol loading, particularly in the BTH.

3.2 Changes in the structural characteristics of precipitation parameters associated with aerosols



288 Fig. 3 illustrates the seasonal mean values of the convective precipitation
 289 parameters for nsRR, STH, LWP, IWP, and PEI across AOD intervals. During spring
 290 (Fig. 3a–e), the BTH and YRD regions exhibit similar responses, with nsRR, STH,
 291 LWP, and PEI demonstrating persistent enhancement as the aerosol burden increases.
 292 In contrast, the YRM and PRD manifest nonlinear features: nsRR, LWP, and IWP
 293 experience initial suppression before rebounding at elevated AOD levels. Summer
 294 observations (Fig. 3f–j) reveal predominantly linear positive relationships between
 295 aerosol loading and precipitation parameters in the BTH, YRD, and YRM regions.
 296 However, the PRD diverges sharply, displaying inverted V-shaped responses in the
 297 nsRR, STH, LWP, and PEI. Autumn analysis (Fig. 3k–o) reveals consistent increases
 298 in the YRM and PRD with aerosol enhancement, whereas the BTH and YRD exhibit
 299 a pattern of initial decline followed by a subsequent increase.

300 The regional comparisons indicate that the differences of the precipitation
 301 parameters are mitigated under moderate to high aerosol loading conditions (Table 1).
 302 For instance, at low aerosol loading, the fractional changes in spring nsRR reach
 303 $\text{DIFF}_{\text{PRD}}=613\%$ and $\text{DIFF}_{\text{YRM}}=247.33\%$, whereas high aerosol loading reduces these
 304 to $\text{DIFF}_{\text{PRD}}=155\%$ and $\text{DIFF}_{\text{YRM}}=49.6\%$ (Table 1). These results highlight that
 305 increasing aerosol loading can moderately alleviate regional disparities in
 306 precipitation characteristics. Furthermore, the BTH exhibits notably higher IWP and
 307 PEI values, indicating enhanced ice-phase processes and superior precipitation
 308 conversion efficiency, as evidenced by the negative DIFF_{YRD} , DIFF_{YRM} , and DIFF_{PRD}
 309 values.



310

311 **Fig. 3.** Average point line plots of nsRR, STH, LWP, IWP, and PEI under three AOD
312 conditions for convective precipitation across the four regions and seasons. Each
313 subplot employs color-coding (BTH–red, YRD–yellow, YRM–green, and
314 PRD–purple) with the x-axis denoting AOD bins ([0,0.3), [0.3,0.6), [0.6, ~)) and the
315 y-axis representing parameter magnitudes.

316



Table 1. Normalized regional differences in convective precipitation during the spring season. Units: nsRR (mm/h), STH (km), LWP (g/m²), IWP (g/m²).

	AOD	BTH	YRD DIFF _{YRD}	YRM DIFF _{YRM}	PRD DIFF _{PRD}
nsRR	[0,0.3)	3	4.23+41.00%	10.42+247.33%	21.4+613.33%
	[0.3,0.6)	3.23	9.1+181.73%	7.75+139.94%	11.76+264.09%
	[0.6,~)	6.19	10.01+61.71%	9.26+49.60%	15.82+155.57%
STH	[0,0.3)	6.99	6.97-0.29%	8.87+26.90%	10.35+48.07%
	[0.3,0.6)	6.79	7.46+9.87%	8+17.82%	9.78+44.04%
	[0.6,~)	7.17	7.44+3.77%	7.93+10.60%	8.93+24.55%
LWP	[0,0.3)	355.11	892.42+151.31%	1593.58+348.76%	3501.97+886.16%
	[0.3,0.6)	414.57	1622.99+291.49%	1242.87+199.80%	2019.85+387.22%
	[0.6,~)	765	1639.19+114.27%	1415.35+85.01%	2407.82+214.75%
IWP	[0,0.3)	584.6	199.12-65.94%	596.38+2.02%	800.57+36.94%
	[0.3,0.6)	466.54	319.12-31.60%	381.24-18.28%	552.17+18.35%
	[0.6,~)	518.72	362.2-30.17%	419.48-19.13%	685.27+32.11%
PEI	[0,0.3)	3.7	3.49-5.68%	4.01+8.38%	4.17+12.70%
	[0.3,0.6)	4.01	3.9-2.74%	4.21+4.99%	3.75-6.48%
	[0.6,~)	4.61	4.27-7.38%	4.37-5.21%	4.33-6.07%

To further characterize the stratiform precipitation parameters (nsRR, STH, LWP, IWP, and PEI), the seasonal mean values across aerosol loading levels are presented in Fig. S4 through point–line plots that were formatted consistently with those in Fig. 3.

For spring (Fig. S4a–e), the BTH, YRD, and YRM exhibit continuously increasing trends in nsRR, LWP, and IWP with increasing aerosol loading. Conversely, the PRD shows overall decreasing trends across most precipitation parameters. In summer (Fig. S4f–j), the BTH, YRD, and YRM demonstrate linear increases in nsRR and LWP means as aerosol loading rises. However, the PRD exhibits nonlinear trends: initial increases followed by decreases in nsRR, STH, LWP, and IWP means, a pattern consistent with its convective precipitation behavior. In autumn (Fig. S4k–o): monotonically rising trends in nsRR, LWP, and IWP are shown



331 by the YRD and YRM, whereas the BTH and PRD display decreasing and then
 332 increasing trends in nsRR, IWP, and PEI, indicating an increase in aerosol loading.
 333 Additionally, the fractional changes in stratiform precipitation indicate that an
 334 increase in aerosol loading moderately reduces regional disparities during regional
 335 normalized difference comparisons, particularly in the spring and summer
 336 (Tables .S3-5). For instance, in the PRD region during spring (Table .S3), the
 337 $DIFF_{PRD}$ values for IWP are 208.16%, 141.06%, and 34.13%, corresponding to AOD
 338 ranges of [0, 0.3), [0.3, 0.6), and [0.6, ~), respectively. The seasonal normalized
 339 differences indicate significant ice-phase processes but weak liquid-phase processes
 340 across various regions during spring.

341 To summarize, aerosols influence the average values of precipitation parameters,
 342 displaying characteristics that differ across spatiotemporal scales and precipitation
 343 types. Furthermore, precipitation parameters exhibit greater regional than seasonal
 344 variation. In particular, within the 270 $DIFF_{region}$ samples, 41 (constituting 15.2%)
 345 exhibited values exceeding 100%, whereas among the 240 $DIFF_{season}$ samples, only 10
 346 (representing 4.2%) demonstrated such a phenomenon (Tables S.1-7). Additionally,
 347 convective precipitation shows larger magnitude changes across seasons and regions
 348 than stratiform precipitation.

349 ***3.3 Changes in the vertical structure of precipitation associated with aerosols***

350 To further investigate the vertical structure of precipitation, Fig. 4 presents the
 351 vertical distributions of the mean Z_e , D_m , N_w , and RR for convective precipitation
 352 under varying AOD loadings and seasons. Overall, the mean Z_e , N_w , and RR values



generally increase with decreasing height, whereas D_m exhibits an initial decrease followed by an increase. In addition, the PRD displays a markedly higher RR than the BTH, YRD, and YRM in spring, but lower RR in summer. This seasonal contrast may be attributed to the abundant moisture supply during the pre-rainy season in South China, versus significant precipitation suppression in summer caused by hygroscopic aerosol-induced moisture competition. Furthermore, Chen et al. (2015) observed that a moderate CAPE in the PRD summer may lead to diminished precipitation.

As shown in Fig. 5a, in spring, the RR and Z_e of BTH, YRD, YRM, and PRD have obvious similarities with the variation in AOD. The RR and Z_e increase linearly with aerosol loading in the BTH and YRD but display non-monotonic trends (initial suppression followed by enhancement) in the YRM and PRD, consistent with Fig. 4a–e. This discrepancy may arise from the predominant influence of DUA on the spring AOD composition of the BTH region (Fig. S1a), whereby their semi-direct effect promotes cloud droplet evaporation, reduces moisture availability, and triggers earlier precipitation (Sun and Zhao, 2021). Although the rising proportion of fine-mode aerosols mitigates dust-induced precipitation suppression as AOD increases, persistently low moisture availability in the BTH maintains precipitation levels below those of the other regions. The YRD exhibits a more abundant water vapor supply (Fig. S1a): Increased aerosol concentrations supply additional CCN and IN, providing more condensation nuclei for cloud droplet formation and thereby enhancing precipitation. With increasing AOD, the YRM transitions from low-concentration coarse particles to high-concentration fine particles (Fig. 4c–d).



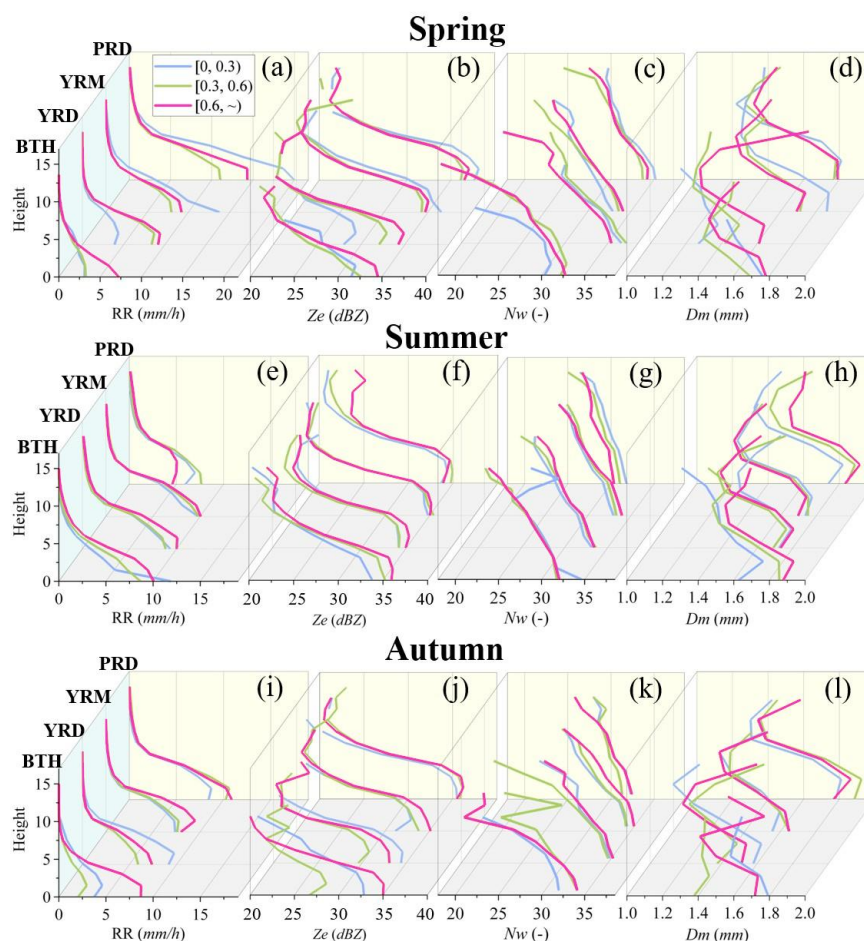
375 Inadequate moisture supply triggers the Twomey effect through competition for cloud
 376 water; however, extended cloud longevity and enhanced collision–coalescence (Fig.
 377 5a) subsequently cause precipitation to initially decline and then rise. The PRD
 378 precipitation patterns resemble those of the YRM, although hygroscopic SSA exert a
 379 stronger influence (Fig. S2a). At low AOD (with an SSA proportion of 26.32%),
 380 moisture from South China's pre-rainy season and hygroscopic giant CCN derived
 381 from sea salt promote spring precipitation growth (Guo et al., 2022). As AOD
 382 increases, the SSA contribution declines rapidly, weakening its
 383 precipitation–promoting effect. However, with further AOD growth, the proportion of
 384 fine (notably hygroscopic OCA) aerosols rises (Fig. S2a), supplying more effective
 385 CCN to enhance the precipitation. Additionally, under low AOD conditions, the lower
 386 atmosphere in the YRD (YRM) is dominated by high concentrations of smaller (larger)
 387 particles. As aerosol loading increases, the Twomey effect emerges in the YRM,
 388 whereas the BTH and YRD exhibit the anti–Twomey effect.

389 During the summer (Fig. 4e–h), average vertical profiles of RR and Z_e in the BTH,
 390 YRD, and YRM generally exhibit increasing linear trends with rising aerosol loading.
 391 Conversely, the PRD shows an initial increase followed by a decrease, which is
 392 consistent with the findings in Fig. 3f–j. Within the BTH, YRD, and YRM, low
 393 proportions of hygroscopic giant CCN (SSA) mean increasing aerosols boost N_w and
 394 D_m , supplying more CCN and IN for cloud droplet formation. Coupled with ample
 395 summer moisture supply and dynamic forcing, cloud droplets are transported to
 396 higher altitudes (Fig. 3g), enhancing precipitation. During summer in the PRD, ample



397 moisture is derived from the Indian Ocean. With low aerosol loading, the proportion
 398 of sea salt particles is elevated (23.83%). An increase in giant sea salt CCN loading
 399 triggers an anti-Twomey effect, characterized by a rise in D_m and a decline in N_w ,
 400 leading to intensified precipitation. Nevertheless, as aerosol loading escalates further,
 401 fine-mode particles predominate (93.9%; Fig. S2b), resulting in moisture competition
 402 becoming the principal mechanism inhibiting precipitation.

403 Consistent with the conclusions in Fig. 3k–o, autumn trends (Fig. 4i–l) show that
 404 precipitation in the BTH and YRD initially decreased and then increased with
 405 increasing aerosol loading, although the magnitude of the increase is increasing with
 406 rising aerosol loading, though the increase magnitude is larger in the BTH than in the
 407 YRD. Conversely, RR exhibits monotonically increasing trends in the YRM and PRD.
 408 The underlying mechanisms are as follows. The BTH and YRD: Initial aerosol
 409 increase elevates N_w while reducing D_m (Fig. 4k–l), suppressing precipitation via the
 410 Twomey effect. However, prolonged cloud lifetime promotes further cloud
 411 development (Fig. 3l–m). Consequently, when aerosol loading continues rising,
 412 abundant CCN and IN become available for cloud–precipitation processes, ultimately
 413 enhancing precipitation. The YRM and PRD: The monotonic trends stem from greater
 414 autumn moisture availability versus the BTH and YRD (Fig. S1c), which supports
 415 cloud droplet condensational growth (Fig. 4k–l) and enhances collision–coalescence
 416 (Fig. 5a), collectively facilitating precipitation.



417

418 **Fig .4.** Vertical profiles of the average convective precipitation parameters Z_e , D_m , N_w
 419 and RR for different regions in different seasons under three AOD conditions
 420 ([0,0.3)–blue lines; [0.3,0.6)–green lines; [0.6, ~)–magenta lines). Within each
 421 subplot, line profiles are categorized into four regions: BTH, YRD, YRM, and PRD.

422 To enhance the characterization of the vertical structure and microphysical
 423 processes of stratiform precipitation, Fig. S5 displays the mean vertical profiles of Z_e ,
 424 D_m , N_w , and RR, similar to those in Fig. 4. A notable Z_e peak at an altitude of 5 km



corresponds to the 0 °C bright band signature, which is a distinctive indicator of the hydrometeor phase transition and stratiform precipitation. Fig. S5a illustrates that the PRD exhibits declining trends in RR and Z_e , diverging from the characteristics of convective precipitation depicted in Fig. 4a–b. In the PRD, increasing aerosol loading induces a Twomey effect: N_w increases, accompanied by a decrease in D_m (Fig. S5c–d). This dominance of particle competition mechanisms at higher AOD loadings aligns with increasing OCA contributions (Fig. S2c–d), as light-absorbing OCAs suppress precipitation via semi-direct effects of shortwave radiation absorption.

During summer (Fig. S5 e–h), the BTH region displayed distinct patterns compared to the other three regions: RR decreases with increasing aerosol loading, whereas Z_e and D_m increase simultaneously. This suggests that higher aerosol loads enhance particle albedo, thereby intensifying the evaporation of smaller particles and the processes of break-up (Fig. 5b), such that while N_w remains stable, the PEI declines (Fig. S4j). Concurrently, the increased abundance of hygroscopic SO₄A further depletes the atmospheric moisture. These combined effects lead to a notable reduction in precipitation within the BTH region. The summer stratiform precipitation responses of the PRD to aerosol loading resemble those of convective precipitation, whereas the YRD and YRM show negligible alterations in the vertical profiles, suggesting a low sensitivity of stratiform precipitation to aerosol loading.

4 Influence of aerosols on precipitation microphysical processes

To validate the aforementioned microphysical processes, this study assesses near-surface precipitation mechanisms below the melting layer. The melting layer



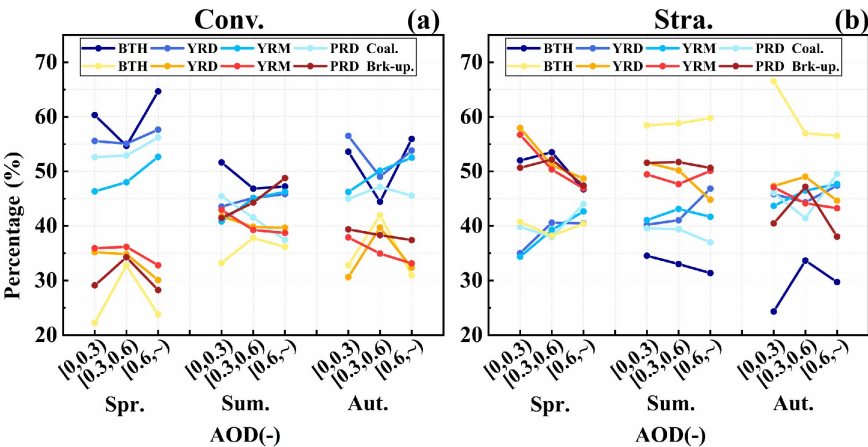
447 refers to the region where the ice phase of the hydrometeors transitions to the liquid
 448 phase during precipitation (Hu et al., 2024), and the analysis employs the
 449 categorization approach established by Kumjian and Prat (2014). This approach
 450 employs radar reflectivity ($\Delta Z_e = Z_e^{1\text{km}} - Z_e^{3\text{km}}$) and raindrop size ($\Delta D_m = D_m^{1\text{km}} - D_m^{3\text{km}}$)
 451 differences between 1 km and 3 km above ground level. These metrics classify
 452 processes into four categories: size sorting evaporation, coalescence, break-up, and
 453 break-up coalescence balance. The extensive application of this methodology
 454 demonstrates that coalescence and break-up processes dominate cloud microphysics
 455 (Chen et al., 2025; Hu et al., 2022; Wen et al., 2023; Zhou et al., 2022).
 456 Consequently, this analysis focuses exclusively on these two mechanisms. Fig. 5
 457 displays the coalescence and break-up processes for convective and stratiform
 458 precipitation across regions and seasons.

459 In convective precipitation (Fig. 5a), coalescence consistently dominates over
 460 break-up across all regions, particularly during spring and autumn. With rising AOD
 461 concentrations, the YRD, YRM, and PRD exhibit enhanced coalescence in spring,
 462 whereas the PRD shows a decreasing-then-increasing trend in coalescence. In summer,
 463 the proportions of coalescence and break-up remain comparable, whereas autumn
 464 exhibits nonlinear responses in the BTH and YRD.

465 In stratiform precipitation (Fig. 5b), break-up generally exceeds coalescence,
 466 with distinct seasonal patterns: in spring, the BTH exhibits increasing-then-decreasing
 467 coalescence, whereas the PRD shows the opposite trend (aligning with divergent RR
 468 patterns in Fig. S5a). During summer and autumn, BTH consistently shows notably



469 lower break-up than coalescence, which is one of the reasons why precipitation
470 continues to decline with increasing AOD loading in summer. The specific
471 microphysical influence process is explained in detail in Section 3.



472
473 **Fig. 5.** Average point line plots of coalescence and break-up processes in precipitation
474 across different regions and seasons (Spr.-Spring, Sum.-Summer, and Aut.-Autumn)
475 under three AOD conditions. Here, (a) represents convective precipitation, and (b)
476 represents stratiform precipitation.

477 **5 Meteorological effects**

478 **5.1 Sensitivity analysis of aerosols to meteorological factors in precipitation**
479 **parameters**

480 Since precipitation processes are equally influenced by thermodynamic and
481 dynamic environments, this study employs RH at 850hPa as a thermal influence
482 factor and CAPE as a dynamic influence factor to examine aerosol sensitivity to these
483 meteorological elements. Following the classification criteria established in Section



484 2.5, RH and CAPE values were categorized into low, medium, and high levels.

485 Following the format of Fig. 3, Fig. 6 displayed point-line plots of convective
 486 precipitation parameters across regions under different RH and aerosol loading
 487 conditions. Notably, higher RH values consistently enhance mean precipitation
 488 parameters (nsRR, LWP, PEI) across all regions, whereas STH and IWP show
 489 inconsistent seasonal and regional variations. This suggests that elevated RH supplies
 490 additional moisture, thereby mitigating moisture competition effects.

491 In spring (Fig. 6a–e), rising RH values do not interfere with the established
 492 trends of the BTH across varying aerosol levels: nsRR and LWP continue to rise with
 493 aerosol loading, yet STH and IWP exhibit persistent decrease-then-increase
 494 trajectories. Precipitation parameters in the YRD and YRM remain consistent with the
 495 characteristics observed in Fig. 3a–e. By contrast, the PRD displays distinct
 496 characteristics under moderate RH conditions. This indicates that aerosols exhibit
 497 greater sensitivity to RH in the spring convective precipitation of the PRD, whereas
 498 aerosol effects dominate over RH influences in the BTH, YRD, and YRM.

499 Summer patterns (Fig. 6f–j) show modified the BTH responses under high RH;
 500 however, other regions remain consistent with prior trends in Fig. 3f–j. In autumn,
 501 observations (Fig. 6k–o) highlight inconsistent aerosol–precipitation relationships
 502 across the RH levels in the PRD. By contrast, the BTH, YRD, and YRM maintain
 503 nearly identical parameter responses.

504 The results indicate that RH sensitivity significantly influences
 505 aerosol-precipitation effects on convective precipitation in the PRD, whereas aerosol



loading is the main factor affecting precipitation parameters in the other three regions.

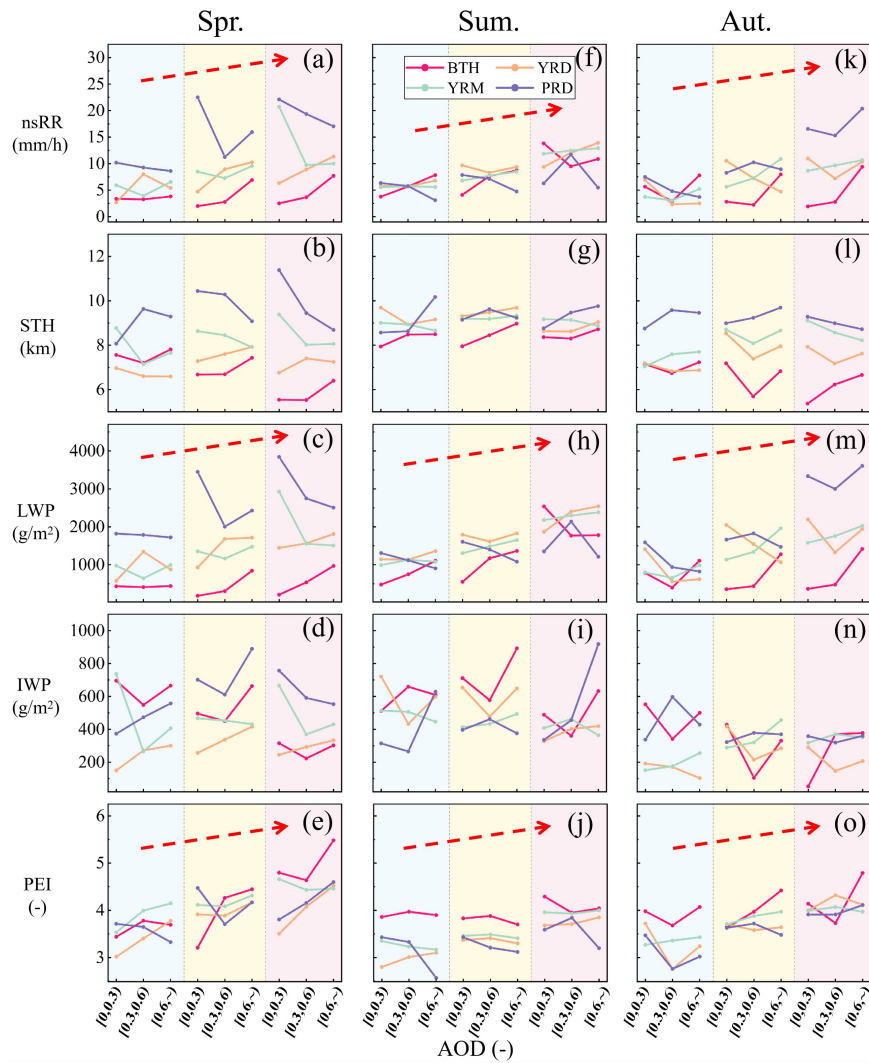


Fig. 6. Point-line graphs of mean values for convective precipitation parameters (nsRR, STH, LWP, IWP, and PEI) across seasons and regions. The analysis is based on three AOD intervals and various RH conditions. Each subpanel displays RH gradients from left to right: low RH (blue background), medium RH (yellow background), and high RH (red background). The red dashed arrow represents the



513 overall variation trend of precipitation parameters with the increase of RH.
514 Fig. S6 presents point-line plots illustrating mean precipitation parameters associated
515 with stratiform precipitation. Increased RH consistently enhances these parameters,
516 particularly nsRR, LWP, and PEI, in BTH, YRD, and YRM. However, the PRD
517 exhibits differing parameter responses across seasons under varying relative humidity
518 conditions, similar to convective precipitation, as aerosol loading rises.

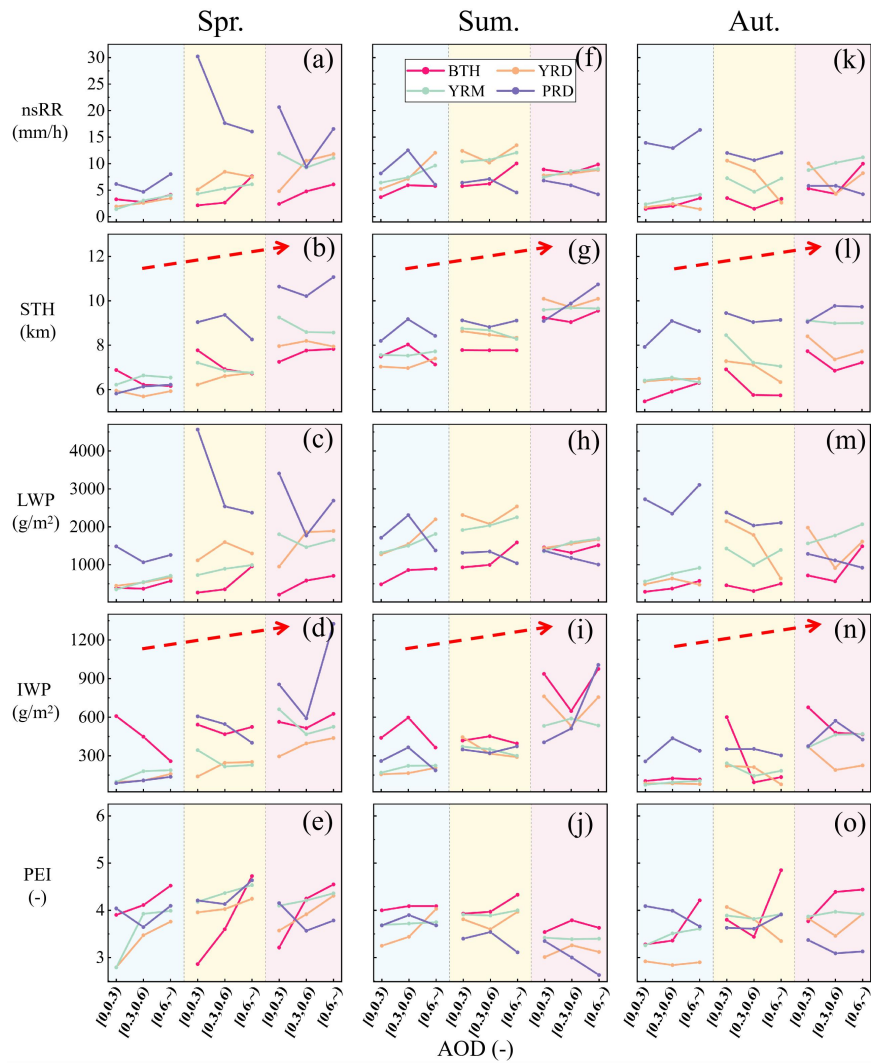
519 In addition to the thermodynamic conditions, CAPE was selected as a dynamic
520 factor. Similar to the RH, the precipitation parameter characteristics across regions
521 were investigated under varying CAPE conditions. As indicated by the red dashed
522 arrows in Fig. 7, increasing CAPE values provide favorable dynamic conditions for
523 convective precipitation, leading to rising STH, increased IWP, and enhanced
524 ice-phase processes.

525 Spring (Fig. 7a–e) shows that in the PRD, the characteristics of nsRR, LWP, and
526 PEI under varying AOD loading remain consistent across different CAPE conditions.
527 In contrast, the BTH, YRD, and YRM exhibit distinct variations in these parameters
528 under different CAPE levels. Summer (Fig. 7f–j) reveals that aerosol effects in the
529 BTH region demonstrate heightened sensitivity to CAPE variations. However, during
530 autumn convective precipitation (Fig. 7k–o), aerosols across the four regions exhibit
531 substantial sensitivity to CAPE, indicating different seasonal response mechanisms to
532 atmospheric instability in these areas.

533 Fig. S7 presents point-line plots of the mean precipitation parameters for
534 stratiform precipitation. Increasing CAPE enhances the STH and IWP parameters,



535 which is consistent with the convective precipitation patterns in Fig. 6.



536
537 **Fig. 7.** Point-line graphs of mean values for convective precipitation parameters
538 across seasons and regions. The analysis is based on three AOD intervals and varying
539 CAPE scenarios. The form of this expression is similar to that shown in Fig. 6.

540 **5.2 Sensitivity analysis of aerosols to meteorological factors in the vertical structure**
541 **of precipitation**



542 Furthermore, to examine aerosol sensitivity to thermodynamic conditions and
 543 their effects on the vertical profiles of precipitation components, mean vertical
 544 profiles of precipitation parameters (Z_e , D_m , N_w , RR) at varying RH levels are
 545 illustrated, according to the technique shown in Fig. 4. Notably, as the parameter
 546 profile variations in Fig. 5 are concentrated within 0–10 km, the vertical coordinate
 547 range is limited to 0–10 km to emphasize the core precipitation processes. Moreover,
 548 where the curves intersect, dashed lines are employed to distinguish the selected
 549 profiles while maintaining the same representational integrity as the solid lines.

550 Spring convective precipitation (Fig. 8a–l) exhibits region-specific responses to
 551 RH, and in the BTH and YRD, increasing RH from low to medium ranges
 552 significantly elevates precipitation under high aerosol loading but suppresses it under
 553 medium loading (Fig. 8a). This discrepancy arises because abundant particles under
 554 elevated RH conditions undergo accelerated condensational growth, which increases
 555 D_m (Fig. 8f). In contrast, the YRM and PRD show that RH enhancement primarily
 556 boosts precipitation, under low aerosol loading (blue curves). This is because in the
 557 YRD and YRM, particle competition continues to dominate at high loading, whereas
 558 added moisture at low loading facilitates condensational growth and enhances N_w (Fig.
 559 8g).

560 For the stratiform precipitation (Fig. 8m–x), the BTH, YRD, and YRM show
 561 consistent rightward shifts in RR curves across aerosol gradients as RH increases.
 562 This suggests that RH enhances moisture availability without modifying
 563 microphysical competition mechanisms. The PRD exhibits a response analogous to its



convective precipitation feature.

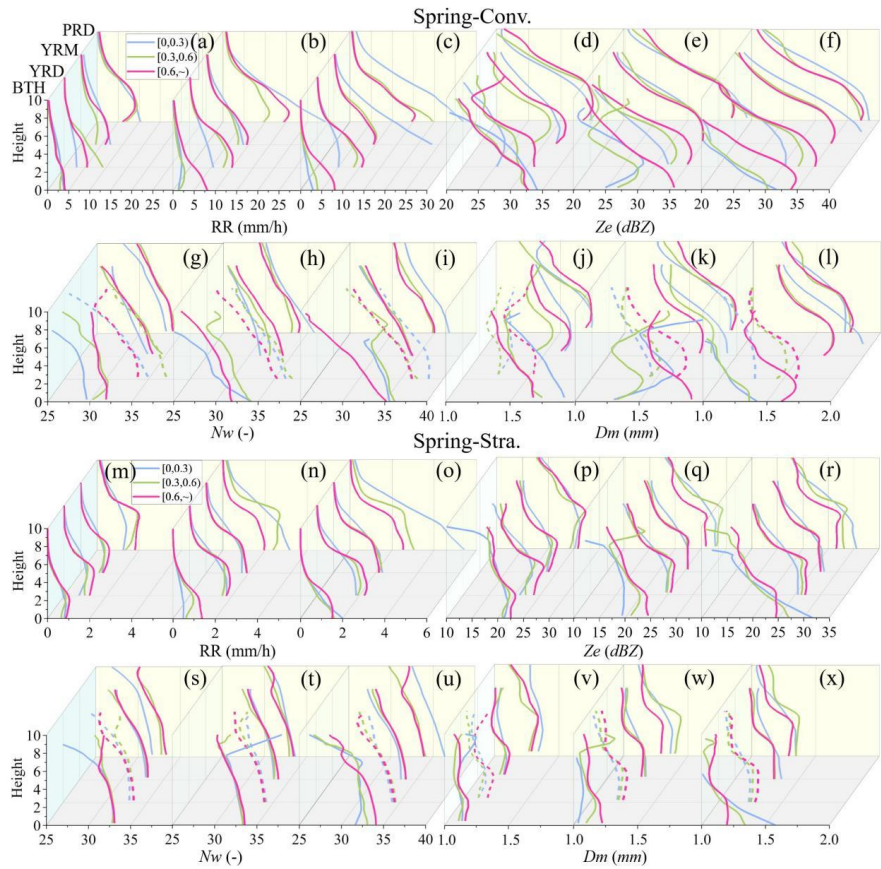


Fig. 8. Vertical profiles of mean precipitation parameters for convective (a–l) and stratiform (m–x) precipitation in spring across four regions. The profiles are shown under three AOD scenarios and RH conditions (arranged left to right as low, medium, high RH; e.g., panels a–c correspond to low, medium, high RH, respectively). To differentiate overlapping curves, selected profiles are plotted as dashed lines while retaining the same representational validity as solid lines.

Additionally, similar characteristics are observed in convective and stratiform precipitation during summer (Figs. S8) and autumn (Figs. S9) with variations in RH.



574 In general, increasing RH provides moisture conditions, accelerates cloud particle
575 condensational growth, and simultaneously increases both D_m and N_w , thereby
576 enhancing precipitation. However, this process also depends on the content of CCN
577 and various physical competition mechanisms.

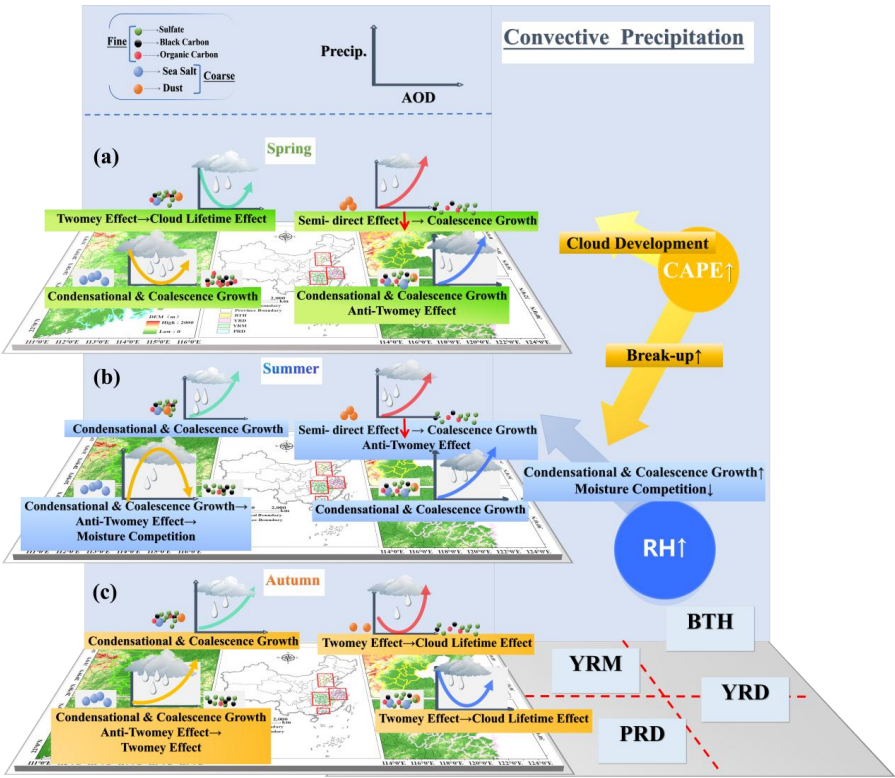
578 Similarly, vertical profiles of precipitation parameters under varying CAPE
579 conditions are presented. Fig. S10 illustrates consistent patterns between convective
580 and stratiform precipitation during spring, echoing the fundamental characteristics in
581 Fig. 8. This consistency suggests that RH and CAPE exert analogous influences on
582 precipitation across aerosol loading gradients during spring.

583 Summer convective precipitation (Fig. S11a–l) reveals distinct regional
584 responses. In the BTH region, CAPE elevation significantly enhances low-AOD
585 precipitation, likely driven by improved dynamic forcing that promotes cloud
586 development (red point line in Fig. S7g). In contrast, the PRD exhibits pronounced
587 precipitation suppression, most evident under moderate aerosol loading, where
588 heightened CAPE intensifies particle break-up processes (Fig. S13h). These findings
589 indicate that RH and CAPE exert divergent influences across regions. For RH,
590 increasing moisture availability promotes particle growth via condensation under
591 suited particle concentrations, but the Twomey effect dominates under high AOD
592 loading, where particle competition for cloud water prevails. CAPE provides
593 favorable dynamic conditions for cloud development, but simultaneously intensifies
594 particle break-up through dynamic forces, which hinders the constant growth of cloud
595 droplets and suppresses precipitation.



596 ***5.3 Sensitivity analysis of aerosols to meteorological factors in precipitation***
597 ***microphysical processes***

598 To validate the aforementioned inferences, the proportions of break-up and
599 coalescence processes in convective and stratiform precipitation are further
600 investigated. Fig. S13 reveals that in convective precipitation, an increase in RH
601 generally correlates with enhanced coalescence (white-green bars in the upper half;
602 the trend is shown by the blue arrows) and reduced break-up (white-green bars in the
603 lower half). Conversely, increasing CAPE is associated with decreased coalescence
604 (green line in the upper half) and intensified break-up (yellow line in the lower half;
605 the trend is shown by the red arrows), particularly in summer and the PRD region. As
606 illustrated in Fig. S14, stratiform precipitation demonstrates similarities to convective
607 precipitation, and the increase in RH makes the enhancement of coalescence
608 processes more universal.



609
610 **Fig. 9.** Theoretical framework of aerosol impact on convective precipitation in the
611 BTH, YRD, YRM, and PRD: (a) spring, (b) summer, and (c) autumn. Symbol
612 conventions, \uparrow : Enhancement of process; \downarrow : Weakening of process; \rightarrow : Transition
613 from left-side process dominance to right-side process dominance; Right-side CAPE
614 arrows: \nearrow promotes precipitation; \searrow suppresses precipitation; Right-side RH arrows:
615 \nearrow enhances precipitation processes. Arrow length reflects the relative process
616 intensity.

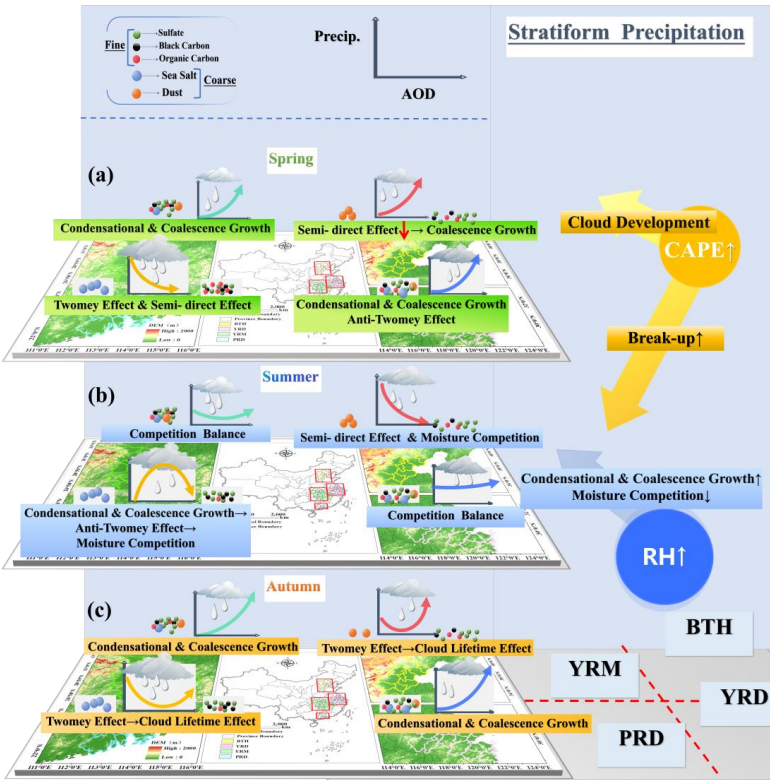


Fig. 10. Theoretical framework of aerosol impact on stratiform precipitation in the BTH, YRD, YRM, and PRD. The form of this expression is similar to that shown in Fig. 9.

6 Conclusion

This study systematically examined the impact of aerosols on precipitation parameters, vertical structures, and microphysical processes in convective and stratiform precipitation across China's four major urban clusters (the BTH, YRD, YRM, and PRD) — during spring, summer, and autumn, utilizing the DPR-MERRA-2-ERA5 dataset. It further explores aerosol sensitivity to RH and CAPE, revealing regional heterogeneity, seasonal dependency, and the underlying



628 microphysical processes of aerosol effects. The research indicates that physical
629 processes, including condensational growth, coalescence growth, semi-direct effects,
630 and moisture competition effects from aerosol-sourced CCN, trigger the Twomey
631 effect, Anti-Twomey effect, and cloud lifetime effect, resulting in varied precipitation
632 alterations. Additionally, an increase in aerosol loading diminishes the regional
633 disparities in precipitation characteristics, with a more pronounced effect during the
634 spring and summer. The precipitation parameters exhibit greater regional variability
635 than seasonal variability, and convective precipitation experiences more significant
636 seasonal and regional changes compared to stratiform precipitation. Based on the
637 findings in Section 3-5, the physical mechanisms by which aerosols at varying
638 concentrations influence convective precipitation (Fig. 9) and stratiform precipitation
639 (Fig. 10) are illustrated, with the following specific conclusions:

640 For convective precipitation (Fig. 9): Precipitation in the BTH region is
641 influenced by seasonal variations in dust aerosols. During spring (Fig. 9a) and
642 summer (Fig. 9b), dust aerosols exert significant impacts, whereas their contributions
643 declines in autumn (Fig. 9c), resulting in distinct precipitation characteristics.
644 Specifically, as the total aerosol concentration increases, the proportion of dust
645 aerosols rapidly decrease. This reduction weakens the semi-direct effect of dust while
646 enhancing the particle coalescence processes, thereby diminishing precipitation
647 suppression. However, insufficient moisture supply and frequent dust events in spring
648 collectively reduce the overall precipitation below the levels observed in the other
649 three regions. In autumn, when the DUA constitutes a minor fraction, rising aerosol



650 concentrations initially suppress precipitation through the Twomey effect, while
651 simultaneously promoting cloud development, subsequently enhancing precipitation
652 through increased CCN availability. The YRD exhibits a persistent precipitation
653 increase with increasing aerosol concentrations owing to the ample moisture supply.
654 While sharing similar seasonal trends with the BTH, its underlying mechanisms differ
655 significantly: abundant water vapor enables continuous precipitation growth during
656 spring (Fig. 9a) and summer (Fig. 9b), primarily attributable to enhanced droplet
657 condensation and coalescence processes. The PRD exhibits the most pronounced
658 seasonal variability, attributable to shifts in the composition of hygroscopic aerosols
659 (SSA). During spring (Fig. 9a), precipitation in the PRD is significantly higher than in
660 other regions under low aerosol loading due to SSAs. As aerosol concentrations
661 increase, diminishing SSA proportion weakens this enhancement until rising
662 hygroscopic organic carbon subsequently reinforces precipitation. In summer (Fig.
663 9b), sufficient moisture initially promotes droplet growth through
664 condensation-coalescence under low aerosol levels. However, the subsequent aerosol
665 accumulation intensifies moisture competition and suppresses precipitation.
666 Monsoon-influenced sea-salt overabundance (Xiao et al., 2025) further amplifies this
667 competition effect, resulting in overall lower precipitation rates compared to other
668 regions.

669 For stratiform precipitation (Fig. 10): Overall, stratiform and convective
670 precipitation share fundamental similarities yet exhibit distinct microphysical
671 processes due to differing cloud formation conditions. With a lower moisture supply



672 than convective systems, stratiform precipitation in the BTH region is suppressed
673 during summer (Fig. 10b) through aerosol semi-direct effects and moisture
674 competition. Similarly, in the PRD, spring precipitation is reduced by organic carbon
675 aerosols (Fig. 10a), which act as both hygroscopic and light-absorbing particles
676 (Zhuang et al., 2025). This occurs when an insufficient moisture supply enhances the
677 radiation-absorbing effect, dominating the precipitation reduction mechanism.

678 Furthermore, variations in RH and CAPE modulate aerosol-precipitation
679 interactions, as shown in Figs. 9–10. Specifically, elevated RH indicates enhanced
680 moisture availability, which facilitates rapid droplet growth through condensation and
681 coalescence under suitable aerosol loading. Regarding dynamic influences, increased
682 CAPE provides favorable conditions for cloud development while simultaneously
683 enhancing droplet break-up through intensified turbulence, hindering cloud droplet
684 growth, and suppressing precipitation, particularly in summer and the PRD region.

685 Overall, aerosol impacts on precipitation result from complex couplings among
686 regional aerosol composition, moisture transport patterns, atmospheric stability, and
687 precipitation types, generating both linear and nonlinear responses. These complex
688 dynamics establish essential theoretical underpinnings for formulating atmospheric
689 cleanup techniques in significant metropolitan centers, enhancing early warning
690 systems for extreme precipitation occurrences, and refining regional climate models.

691

692

693



694 **7 Discussion**

695 Building on the findings of Peng et al. (2025), which investigated the effects of
696 fine and coarse aerosols on summer precipitation structure and microphysics in the
697 YRD region, the present study expands the scope of analysis to examine aerosol
698 impacts on precipitation vertical structures and microphysical processes across
699 multiple regions and seasons in China. This extended scope has led to the following
700 new findings: (1)Enhanced aerosol loading reduces regional precipitation disparities,
701 most pronounced in spring and summer. (2)Precipitation exhibits stronger regional
702 than seasonal variability. (3)The BTH precipitation is dominated by dust aerosols,
703 whereas the YRD and PRD are influenced by sea salt aerosols. These conclusions are
704 primarily derived from analyses of satellite-based datasets, which provide extensive
705 spatial coverage, high spatiotemporal resolution, and continuous temporal monitoring.
706 Nevertheless, it is important to acknowledge that considerable uncertainties persist in
707 satellite data processing and retrieval algorithms, especially under complex
708 atmospheric and surface conditions. Additionally, spatiotemporal resolution and
709 format discrepancies across multisource data introduce unavoidable uncertainties.
710 This study primarily focuses on the vertical structural characteristics of precipitation,
711 whereas the analysis of aerosol data lacks comprehensive three-dimensional matching.
712 Currently, vertical profiling of aerosols relies primarily on aircraft sounding (Zhou et
713 al., 2023) and simulated radar signals (Fajardo-Zambrano et al., 2022), which remain
714 spatially limited. Satellite remote sensing is hindered by inadequate resolution and
715 deficiency in three-dimensional information (Li et al., 2022). However, the successful



716 launch and stable operation of EarthCARE now facilitates accurate three-dimensional
717 vertical profiling of clouds and aerosols via lidar (ATLID) and cloud profiling radar
718 (CPR) (Irbah et al., 2023). Future collaborative observations from the GPM and
719 EarthCARE will produce enhanced datasets on clouds, precipitation, and aerosols,
720 thus facilitating more robust in-depth studies within this research framework.
721 Subsequent research should integrate supplementary meteorological variables and
722 machine-learning methodologies to more effectively delineate aerosol effects and
723 examine their responsiveness to meteorological influences. Notably, as Zhao et
724 al.(2025) revealed distinct aerosol-cloud interaction patterns over land versus ocean
725 in the YRD, the absence of cloud parameter products in this study may inherently
726 limit the depth of the aerosol-precipitation mechanism analysis. This methodological
727 constraint thus necessitates the future integration of high-resolution cloud parameter
728 datasets to refine research findings, enabling a comprehensive exploration of
729 aerosol-cloud-precipitation coupling mechanisms, specifically encompassing dry and
730 wet aerosol removal processes and precipitation feedback loops.

731 **Data availability**

732 The V07A GPM 2ADPR products used in this paper are openly available at the
733 NASA Goddard Space Flight Center's Precipitation Processing System (PPS) team
734 (<https://storm.pps.eosdis.nasa.gov/storm/>).

735 **Author contributions**

736 H P & Z L: Writing – review & editing, Writing – original draft, Visualization,
737 Validation, Methodology, Investigation. X H: Writing – original draft, Validation,



738 Supervision, Software, Resources, Methodology, Investigation, Formal analysis, Data
739 curation, Conceptualization. W A: Writing – review & editing, Project administration.
740 S H & J Q: Writing – review & editing, Investigation. X Z: Writing – review &
741 editing, Funding acquisition, Formal analysis.

742 **Declaration of competing interest**

743 The authors declare that they have no known competing financial interests or
744 personal relationships that could have appeared to influence the work reported in this
745 paper.

746 **Acknowledgments**

747 Zhen Li and Heyuan Peng contributed equally to this work and should be
748 considered as co-first authors. The authors thank the anonymous reviewers for their
749 constructive comments and suggestions, which have greatly improved the quality of
750 this paper.

751 **Financial support**

752 This work has been jointly supported by the National Natural Science
753 Foundation of China (grant nos. 42305150).

754

755 **References**

- 756 Ackerman, A. S., Toon, O. B., Stevens, D. E., Heymsfield, A. J., Ramanathan, V., and
757 Welton, E. J.: Reduction of Tropical Cloudiness by Soot, Science, Vol.288,
758 1042–1047, <https://doi.org/10.1126/science.288.5468.1042>, 2000.
- 759 Albrecht, B. A.: Aerosols, Cloud Microphysics, and Fractional Cloudiness, Science,



- 760 245, 1227–1230, <https://doi.org/10.1126/science.245.4923.1227>, 1989.
- 761 Buchard, V., Randles, C. A., Da Silva, A. M., Darmenov, A., Colarco, P. R.,
 762 Govindaraju, R., Ferrare, R., Hair, J., Beyersdorf, A. J., Ziemba, L. D., and Yu,
 763 H.: The MERRA-2 aerosol reanalysis, 1980 onward. Part II: Evaluation and case
 764 studies, *J. Climate*, 30, 6851–6872, <https://doi.org/10.1175/JCLI-D-16-0613.1>,
 765 2017.
- 766 Chandrasekar, V. and Le, M.: Evaluation of profile classification module of
 767 GPM-DPR algorithm after launch, in: 2015 IEEE International Geoscience and
 768 Remote Sensing Symposium (IGARSS), IGARSS 2015 - 2015 IEEE
 769 International Geoscience and Remote Sensing Symposium, Milan, Italy,
 770 5174–5177, <https://doi.org/10.1109/igarss.2015.7326999>, 2015.
- 771 Chang, D., Cheng, Y., Reutter, P., Trentmann, J., Burrows, S. M., Spichtinger, P.,
 772 Nordmann, S., Andreae, M. O., Pöschl, U., and Su, H.: Comprehensive mapping
 773 and characteristic regimes of aerosol effects on the formation and evolution of
 774 pyro-convective clouds, *Atmos. Chem. Phys.*, 15, 10325–10348,
 775 <https://doi.org/10.5194/acp-15-10325-2015>, 2015.
- 776 Chen, F., Yang, Y., Yu, L., Li, Y., Liu, W., Liu, Y., and Lolli, S.: Distinct effects of fine
 777 and coarse aerosols on microphysical processes of shallow-precipitation systems
 778 in summer over southern China, *Atmos. Chem. Phys.*, 25, 1587–1601,
 779 <https://doi.org/10.5194/acp-25-1587-2025>, 2025.
- 780 Dong, X., Li, R., Wang, Y., Fu, Y., and Zhao, C.: Potential impacts of sahara dust
 781 aerosol on rainfall vertical structure over the atlantic ocean as identified from
 782 EOF analysis, *JGR Atmospheres*, 123, 8850–8868,
 783 <https://doi.org/10.1029/2018JD028500>, 2018.
- 784 Fajardo-Zambrano, C. M., Bravo-Aranda, J. A., Granados-Muñoz, M. J.,
 785 Montilla-Rosero, E., Casquero-Vera, J. A., Rejano, F., Castillo, S., and
 786 Alados-Arboledas, L.: Lidar and Radar Signal Simulation: Stability Assessment
 787 of the Aerosol–Cloud Interaction Index, *Remote Sensing*, 14, 1333,
 788 <https://doi.org/10.3390/rs14061333>, 2022.
- 789 Fan, J., Zhang, R., Li, G., and Tao, W.: Effects of aerosols and relative humidity on
 790 cumulus clouds, *J. Geophys. Res.*, 112, <https://doi.org/10.1029/2006jd008136>,
 791 2007.
- 792 Gettelman, A.: Putting the clouds back in aerosol–cloud interactions, *Atmos. Chem.*
 793 *Phys.*, 15, 12397–12411, <https://doi.org/10.5194/acp-15-12397-2015>, 2015.
- 794 Guo, J., Liu, H., Li, Z., Rosenfeld, D., Jiang, M., Xu, W., Jiang, J. H., He, J., Chen, D.,
 795 Min, M., and Zhai, P.: Aerosol-induced changes in the vertical structure of
 796 precipitation: a perspective of TRMM precipitation radar, *Atmos. Chem. Phys.*,



- 18, 13329–13343, <https://doi.org/10.5194/acp-18-13329-2018>, 2018.
- Guo, J., Luo, Y., Yang, J., Furtado, K., and Lei, H.: Effects of anthropogenic and sea salt aerosols on a heavy rainfall event during the early-summer rainy season over coastal Southern China, *Atmospheric Research*, 265, 105923, <https://doi.org/10.1016/j.atmosres.2021.105923>, 2022.
- Hersbach, H., Bell, B., Berrisford, P., Hirahara, S., Horányi, A., Muñoz-Sabater, J., Nicolas, J., Peubey, C., Radu, R., Schepers, D., Simmons, A., Soci, C., Abdalla, S., Abellan, X., Balsamo, G., Bechtold, P., Biavati, G., Bidlot, J., Bonavita, M., De Chiara, G., Dahlgren, P., Dee, D., Diamantakis, M., Dragani, R., Flemming, J., Forbes, R., Fuentes, M., Geer, A., Haimberger, L., Healy, S., Hogan, R. J., Hólm, E., Janisková, M., Keeley, S., Laloyaux, P., Lopez, P., Lupu, C., Radnoti, G., De Rosnay, P., Rozum, I., Vamborg, F., Villaume, S., and Thépaut, J.: The ERA5 global reanalysis, *Quart J Royal Meteorol Soc*, 146, 1999–2049, <https://doi.org/10.1002/qj.3803>, 2020.
- Hou, A. Y., Kakar, R. K., Neeck, S., Azarbarzin, A. A., Kummerow, C. D., Kojima, M., Oki, R., Nakamura, K., and Iguchi, T.: The Global Precipitation Measurement Mission, *Bull. Amer. Meteor. Soc.*, 95, 701–722, <https://doi.org/10.1175/bams-d-13-00164.1>, 2014.
- Hu, X., Ai, W., Qiao, J., Hu, S., Han, D., and Yan, W.: Microphysics of Summer Precipitation Over Yangtze-Huai River Valley Region in China Revealed by GPM DPR Observation, *Earth and Space Science*, 9, <https://doi.org/10.1029/2021ea002021>, 2022.
- Hu, X., Ai, W., Qiao, J., and Yan, W.: Insight into global climatology of melting layer: Latitudinal dependence and orographic relief, *Theor Appl Climatol*, 155, 4863–4873, <https://doi.org/10.1007/s00704-024-04926-6>, 2024.
- Huang, J., Wang, T., Wang, W., Li, Z., and Yan, H.: Climate effects of dust aerosols over East Asian arid and semiarid regions, *JGR Atmospheres*, 119, <https://doi.org/10.1002/2014jd021796>, 2014.
- IPCC. 2013. Climate Change 2013: The Physical Science Basis. Contribution of Working Group I to the Fifth Assessment Report of the Intergovernmental Panel on Climate Change [M]. Stocker TF, Qin D, Plattner G K, et al., Eds. Cambridge, United Kingdom and New York, NY, USA: Cambridge University Press, 1535pp.
- IPCC. 2021. Climate Change 2021: The Physical Science Basis. Contribution of Working Group I to the Sixth Assessment Report of the Intergovernmental Panel on Climate Change [M]. Masson-Delmotte V, Zhai P, Pirani A, et al., Eds. Cambridge, United Kingdom and New York, NY, USA: Cambridge University Press, 2338pp.



- 834
 835 Irbah, A., Delanoë, J., Van Zadelhoff, G.-J., Donovan, D. P., Kollias, P.,
 836 Puigdomènech Treserras, B., Mason, S., Hogan, R. J., and Tatarevic, A.: The
 837 classification of atmospheric hydrometeors and aerosols from the EarthCARE
 838 radar and lidar: the A-TC, C-TC and AC-TC products, *Atmos. Meas. Tech.*, 16,
 839 2795–2820, <https://doi.org/10.5194/amt-16-2795-2023>, 2023.
- 840 Ji, Z. and Tian, S.: A novel potential cause of extreme precipitation in the northwest
 841 China, *Heliyon*, 10, e30826, <https://doi.org/10.1016/j.heliyon.2024.e30826>,
 842 2024.
- 843 Jiang, M., Li, Y., Hu, W., Yang, Y., Brasseur, G., and Zhao, X.: Model-based insights
 844 into aerosol perturbation on pristine continental convective precipitation, *Atmos.*
 845 *Chem. Phys.*, 23, 4545–4557, <https://doi.org/10.5194/acp-23-4545-2023>, 2023.
- 846 Kotsuki, S., Terasaki, K., Satoh, M., and Miyoshi, T.: Ensemble-based data
 847 assimilation of GPM DPR reflectivity: Cloud microphysics parameter estimation
 848 with the nonhydrostatic icosahedral atmospheric model (NICAM), *Journal of*
 849 *Geophysical Research: Atmospheres*, 128, <https://doi.org/10.1029/2022jd037447>,
 850 2023.
- 851 Kumjian, M. R. and Prat, O. P.: The Impact of Raindrop Collisional Processes on the
 852 Polarimetric Radar Variables, *Journal of the Atmospheric Sciences*, 71,
 853 3052–3067, <https://doi.org/10.1175/jas-d-13-0357.1>, 2014.
- 854 Lasser, M., O, S., and Foelsche, U.: Evaluation of GPM-DPR precipitation estimates
 855 with WegenerNet gauge data, *Atmos. Meas. Tech.*, 12, 5055–5070,
 856 <https://doi.org/10.5194/amt-12-5055-2019>, 2019.
- 857 Li, J., Carlson, B. E., Yung, Y. L., Lv, D., Hansen, J., Penner, J. E., Liao, H.,
 858 Ramaswamy, V., Kahn, R. A., Zhang, P., Dubovik, O., Ding, A., Lacis, A. A.,
 859 Zhang, L., and Dong, Y.: Scattering and absorbing aerosols in the climate system,
 860 *Nat Rev Earth Environ*, 3, 363–379, <https://doi.org/10.1038/s43017-022-00296-7>,
 861 2022.
- 862 Li, Z., Lau, W. K.-M., Ramanathan, V., Wu, G., Ding, Y., Manoj, M. G., Liu, J., Qian,
 863 Y., Li, J., Zhou, T., Fan, J., Rosenfeld, D., Ming, Y., Wang, Y., Huang, J., Wang,
 864 B., Xu, X., Lee, S.-S., Cribb, M., Zhang, F., Yang, X., Zhao, C., Takemura, T.,
 865 Wang, K., Xia, X., Yin, Y., Zhang, H., Guo, J., Zhai, P. M., Sugimoto, N., Babu,
 866 S. S., and Brasseur, G. P.: Aerosol and monsoon climate interactions over asia,
 867 *Reviews of Geophysics*, 54, 866 – 929, <https://doi.org/10.1002/2015RG000500>,
 868 2016.
- 869 Li, Z., Wang, Y., Guo, J., Zhao, C., Cribb, M. C., Dong, X., Fan, J., Gong, D., Huang,
 870 J., Jiang, M., Jiang, Y., Lee, S.-S., Li, H., Li, J., Liu, J., Qian, Y., Rosenfeld, D.,
 871 Shan, S., Sun, Y., Wang, H., Xin, J., Yan, X., Yang, X., Yang, X., Zhang, F., and



- 872 Zheng, Y.: East asian study of tropospheric aerosols and their impact on regional
873 clouds, precipitation, and climate (EAST-AIRCPC), *Journal of Geophysical*
874 *Research: Atmospheres*, 124, 13026 – 13054,
875 <https://doi.org/10.1029/2019JD030758>, 2019.
- 876 Liu, C. and Zipser, E. J.: The global distribution of largest, deepest, and most intense
877 precipitation systems, *Geophysical Research Letters*, 42, 3591–3595,
878 <https://doi.org/10.1002/2015gl063776>, 2015.
- 879 Liu, Y., De Leeuw, G., Kerminen, V.-M., Zhang, J., Zhou, P., Nie, W., Qi, X., Hong, J.,
880 Wang, Y., Ding, A., Guo, H., Krüger, O., Kulmala, M., and Petäjä, T.: Analysis of
881 aerosol effects on warm clouds over the Yangtze River Delta from multi-sensor
882 satellite observations, *Atmos. Chem. Phys.*, 17, 5623–5641,
883 <https://doi.org/10.5194/acp-17-5623-2017>, 2017.
- 884 Peng, H., Hu, X., Ai, W., Qiao, J., and Zhao, X.: Effects of fine and coarse aerosols on
885 the summer precipitation structure and microphysics over the yangtze river delta
886 region, *Atmospheric Research*, 326, 108277,
887 <https://doi.org/10.1016/j.atmosres.2025.108277>, 2025.
- 888 Pravia-Sarabia, E., Montávez, J. P., Halifa-Marin, A., Jiménez-Guerrero, P., and
889 Gomez-Navarro, J. J.: The role of aerosol concentration on precipitation in a
890 winter extreme mixed-phase system: The case of storm filomena, *Remote*
891 *Sensing*, 15, 1398, <https://doi.org/10.3390/rs15051398>, 2023.
- 892 Ramanathan, V., Crutzen, P. J., Kiehl, J. T., and Rosenfeld, D.: Aerosols, Climate, and
893 the Hydrological Cycle, *Science*, 294, 2119–2124,
894 <https://doi.org/10.1126/science.1064034>, 2001.
- 895 Rosenfeld, D., Lohmann, U., Raga, G. B., O'Dowd, C. D., Kulmala, M., Fuzzi, S.,
896 Reissell, A., and Andreae, M. O.: Flood or Drought: How Do Aerosols Affect
897 Precipitation?, *Science*, 321, 1309–1313,
898 <https://doi.org/10.1126/science.1160606>, 2008.
- 899 Snively, D. V. and Gallus, W. A.: Prediction of Convective Morphology in
900 Near-Cloud-Permitting WRF Model Simulations, *Weather and Forecasting*, 29,
901 130–149, <https://doi.org/10.1175/waf-d-13-00047.1>, 2014.
- 902 Storer, R. L., Van Den Heever, S. C., and Stephens, G. L.: Modeling Aerosol Impacts
903 on Convective Storms in Different Environments, *Journal of the Atmospheric*
904 *Sciences*, 67, 3904–3915, <https://doi.org/10.1175/2010jas3363.1>, 2010.
- 905 Sun, N., Fu, Y., Zhong, L., and Li, R.: Aerosol effects on the vertical structure of
906 precipitation in east China, *npj Clim Atmos Sci*, 5, 60,
907 <https://doi.org/10.1038/s41612-022-00284-0>, 2022.
- 908 Sun, Y. and Zhao, C.: Distinct impacts on precipitation by aerosol radiative effect over



- 909 three different megacity regions of eastern China, *Atmos. Chem. Phys.*, 21,
 910 16555–16574, <https://doi.org/10.5194/acp-21-16555-2021>, 2021.
- 911 Sun, Y., Dong, X., Cui, W., Zhou, Z., Fu, Z., Zhou, L., Deng, Y., and Cui, C.: Vertical
 912 Structures of Typical Meiyu Precipitation Events Retrieved From GPM-DPR,
 913 *JGR Atmospheres*, 125, <https://doi.org/10.1029/2019jd031466>, 2020.
- 914 Sun, Y., Wang, Y., Zhao, C., Zhou, Y., Yang, Y., Yang, X., Fan, H., Zhao, X., and Yang,
 915 J.: Vertical Dependency of Aerosol Impacts on Local Scale Convective
 916 Precipitation, *Geophysical Research Letters*, 50,
 917 <https://doi.org/10.1029/2022gl102186>, 2023.
- 918 Twomey, S.: Pollution and the planetary albedo, *Atmospheric Environment* (1967), 8,
 919 1251–1256, [https://doi.org/10.1016/0004-6981\(74\)90004-3](https://doi.org/10.1016/0004-6981(74)90004-3), 1974.
- 920 Wen, L., Chen, G., Yang, C., Zhang, H., and Fu, Z.: Seasonal variations in
 921 precipitation microphysics over East China based on GPM DPR observations,
 922 *Atmospheric Research*, 293, 106933,
 923 <https://doi.org/10.1016/j.atmosres.2023.106933>, 2023.
- 924 Xiao, Y., Zhang, J., Zhu, J., and Dai, Q.: Exploration of aerosol-precipitation
 925 relationships under different climate regimes in China, *GIScience & Remote*
 926 *Sensing*, 62, <https://doi.org/10.1080/15481603.2025.2457992>, 2025.
- 927 Xie, X., Liu, X., Peng, Y., Wang, Y., Yue, Z., and Li, X.: Numerical simulation of
 928 clouds and precipitation depending on different relationships between aerosol
 929 and cloud droplet spectral dispersion, *Tellus B: Chemical and Physical*
 930 *Meteorology*, 65, 19054, <https://doi.org/10.3402/tellusb.v65i0.19054>, 2013.
- 931 Yu, H.-R., Zhang, Y.-L., Cao, F., Yang, X.-Y., Xie, T., Zhang, Y.-X., and Xue, Y.:
 932 Gas-to-particle partitioning of atmospheric water-soluble organic aerosols:
 933 Indications from high-resolution observations of stable carbon isotope,
 934 *Atmospheric Environment*, 327, 120494,
 935 <https://doi.org/10.1016/j.atmosenv.2024.120494>, 2024.
- 936 Zhai, H., Yao, J., Wang, G., and Tang, X.: Spatio-Temporal Characteristics and
 937 Variation Pattern of the Atmospheric Particulate Matter Concentration: A Case
 938 Study of the Beijing–Tianjin–Hebei Region, China, *Atmosphere*, 13, 120,
 939 <https://doi.org/10.3390/atmos13010120>, 2022.
- 940 Zhang, J., Gao, Z., and Li, Y.: Deep-Learning Correction Methods for Weather
 941 Research and Forecasting (WRF) Model Precipitation Forecasting: A Case Study
 942 over Zhengzhou, China, *Atmosphere*, 15, 631,
 943 <https://doi.org/10.3390/atmos15060631>, 2024.
- 944 Zhao, C., Sun, Y., Yang, J., Li, J., Zhou, Y., Yang, Y., Fan, H., and Zhao, X.:
 945 Observational evidence and mechanisms of aerosol effects on precipitation,



- 946 Science Bulletin, 69, 1569–1580, <https://doi.org/10.1016/j.scib.2024.03.014>,
 947 2024.
- 948 Zhao, J., Li, T., Shi, K., Qiao, Z., and Xia, Z.: Evaluation of ERA-5 precipitable water
 949 vapor data in plateau areas: A case study of the northern qinghai-tibet plateau,
 950 Atmosphere, 12, 1367, <https://doi.org/10.3390/atmos12101367>, 2021.
- 951 Zhao, X., Zhao, C., Chi, Y., Yang, J., Sun, Y., Yang, Y., and Fan, H.: Different Impacts
 952 of Aerosols on Cloud Development over Land and Ocean Regions in East China,
 953 Adv. Atmos. Sci., 42, 731–743, <https://doi.org/10.1007/s00376-024-4165-z>,
 954 2025.
- 955 Zhou, J., Zhao, W., Fang, B., Xu, X., Wang, S., Liu, Q., Zhang, W., and Chen, W.:
 956 Unmanned-aerial-vehicle-borne cavity enhanced albedometer: A powerful tool
 957 for simultaneous in-situ measurement of aerosol light scattering and absorption
 958 vertical profiles, Opt. Express, 31, 20518, <https://doi.org/10.1364/oe.493696>,
 959 2023.
- 960 Zhou, L., Xu, G., Xiao, Y., Wan, R., Wang, J., and Leng, L.: Vertical structures of
 961 abrupt heavy rainfall events over southwest China with complex topography
 962 detected by dual-frequency precipitation radar of global precipitation
 963 measurement satellite, Intl Journal of Climatology, 42, 7628–7647,
 964 <https://doi.org/10.1002/joc.7669>, 2022.
- 965 Zhuang, Y., Lin, T., Zhou, W., Guo, Z., and Wang, F.: Characteristics of temporal
 966 variations in organic and elemental carbon aerosols from Eastern China in
 967 2011–2020, Journal of Environmental Sciences, 155, 583–596,
 968 <https://doi.org/10.1016/j.jes.2024.05.037>, 2025.

969